Absence of Local Retinotopy in the Mouse Optic Tract

Authors: Matteo Tripodi[1], Hiroki Asari*[1]

Affiliations:

1. Epigenetics and Neurobiology Unit, EMBL Rome, European Molecular Biology Laboratory, Monterotondo, 00015, Italy

***Corresponding author:** Hiroki Asari, E-mail: asari@embl.it

Author contributions: M.T. collected the experimental data; H.A. designed the study, analyzed the data, and wrote the manuscript.

Competing interests: The authors declare no competing financial interests.

Key words: retinotopy; optic tract; retinal ganglion cells; lateral geniculate nucleus

Acronyms: AP, anterior-posterior; DV, dorsal-ventral; IR, infrared; LED, light emitting diode; LGN, lateral geniculate nucleus; ML, medial-lateral; OT, optic tract; PFA, paraformaldehyde; RF, receptive field; RGC, retinal ganglion cell; STA, spike-triggered average; UV, ultraviolet.

Acknowledgements: This work was supported by research grants from EMBL (H.A.). The EMBL Light Imaging Facility is acknowledged for support in histological image acquisition; EMBL IT Support for provision of computer and data storage servers; and the LAR facility for taking care of animals. We thank all the Asari lab members for useful discussions.

Abstract

Retinotopy is a fundamental organizational principle of the visual system, where neighboring neurons represent adjacent points in visual space. This spatial relationship is established by precise anatomical wiring across successive areas, from the retina to the lateral geniculate nucleus (LGN) to the visual cortex. To examine the precision of this topographic arrangement within the long-range projection axons themselves, we recorded retinal ganglion cell (RGC) axons in the mouse optic tract (OT) and mapped their receptive fields (RFs). As expected for a retinotopically organized area, we found that nearby LGN cell pairs had significantly smaller RF distances than distant pairs. In contrast, no such relationship was observed among RGC axons in the OT. Modelling analyses further confirmed that the observed RF distances in the OT were incompatible with any locally retinotopic arrangement. Instead, the OT retained only coarse topography, with ~20° RF deviations or ~45 μm axonal displacements from an ideal retinotopic organization. These results demonstrate that the mouse OT lacks fine-scale retinotopy and maintains only broad topographic structure.

Introduction

The vertebrate visual system maintains spatial relationships from the retina to the downstream visual areas via topographic projections (Huberman et al., 2008; Seabrook et al., 2017; Cang et al., 2018). This retinotopic organization emerges early in development (Debski and Cline, 2002; McLaughlin and O'Leary, 2005; Cang and Feldheim, 2013), and provides a fundamental platform for visual processing, ensuring that nearby points in visual space are represented by neighboring neuronal populations. In the mouse, retinal ganglion cells (RGCs) project to >40 brain areas (Morin and Studholme 2014; Martersteck et al, 2017), with nearly all axons passing through the same pathway – the optic nerve, optic chiasm, and optic tract (OT) – before diverging to structures, such as the superior colliculus and the lateral geniculate nucleus (LGN). While retinotopy in these target areas has been well characterized (McLaughlin, et al., 2003; Piscopo et al., 2013; Molotkov et al., 2023), it remains elusive to what extent retinotopy is maintained in the long-range RGC axons themselves.

Previous anatomical and tracing studies have demonstrated that retinotopy is largely preserved in the optic nerve (Bunt and Horder, 1983; Reese, 2011; but see Horton et al. 1979). Axons arising from specific retinal quadrants occupy consistent positions within the optic nerve, forming a reliable mapping of the retinal geometry as they exit the eye. This topographic organization is, however, substantially disrupted in the optic chiasm (Marcus and Mason, 1995; Colerro and Guillery, 1998), where axons from the two eyes intersect and distribute themselves into either ipsilateral or contralateral side. The optic chiasm has thus been considered as a sorting hub, where retinotopy is relaxed to permit reorganization based on molecular cues, midline crossing decision, and eventual target-specific routing (Jeffery, 2001). After passing through the optic chiasm, RGC axons reorganize and partially recover retinotopic organization in the OT (Plas et al., 2005; Sitko et al., 2018). Such pre-target axon sorting has been widely observed across the brain, including the olfactory nerve (Imai, et al., 2009) and the corpus callosum (Zhou et al., 2013). This indicates the presence of coarse retinotopy in the OT before reaching the target; however, questions remain on the precision and functional consequences of this reorganization.

Using in vivo electrophysiological recordings, here we mapped visual receptive fields (RFs) of individual RGC axons in the mouse OT. We quantified the spatial organization of these RFs, and took a data-driven modelling approach to evaluate how faithfully visual space is represented in the OT. Our results revealed a moderate degree of retinotopy, but not a fine-grained one. This highlights a robustness of the visual system to imprecision in long-range wiring, with refinement of the topographic organization taking place in each target area.

Results

In a brain region with retinotopy, by definition, neighboring cells have adjacent receptive fields (RFs), representing nearby points in visual space (Cang and Feldheim, 2013; Seabrook et al., 2017). To examine if the optic tract (OT) has a retinotopic organization, we thus performed in vivo extracellular recordings of retinal ganglion cell (RGC) axons in the mouse OT, and

54 mapped their RFs using white noise stimuli and reverse correlation (e.g., **Fig. 1A-E**). As a
55 positive control, recordings were also made from the dorsal lateral geniculate nucleus (LGN;
56 e.g., **Fig. 1F-J**), a major retinorecipient area well-known to have a retinotopy (Piscopo, et al.,
57 2013).

58 Using multichannel silicon probes (4 shanks, each with 8-16 recording sites; **Fig. 1**),
59 we simultaneously recorded 6±4 single-units from the OT (mean ± standard deviation, 33
60 animals) and 17±16 single-units from the LGN (17 animals). We found that the measured RFs
61 of those single-units from the OT recordings were widely distributed across the visual
62 stimulation area (73° and 44° in azimuth and elevation, respectively; e.g., **Fig. 1E**). This was
63 also the case even for those units that had the largest signals on the same recording site,
64 hence were supposedly located near each other in close proximity to the recording site (e.g.,
65 **Fig. 1B-D**). In contrast, the measured RFs of LGN cells were spatially more clustered (e.g.,
66 **Fig. 1J**) and demonstrated substantial overlap, especially among neighboring cells (e.g., **Fig.**
67 **1G-I**) as expected from the presence of retinotopy in LGN (Huberman et al., 2008 ; Seabrook
68 et al., 2017). Such qualitative differences in the RF spatial organization between LGN and OT
69 suggest that retinotopy does not exist in the mouse OT.

70 For quantitative population-level data analysis, we calculated the RF distance between
71 every pair of simultaneously recorded single-units, and compared it between nearby and
72 distant cell pairs (**Fig. 2**). Here, we defined nearby cell pairs as those single-units that had the
73 largest signals on the same recording site, whereas distant pairs as those with the largest
74 signals on different recordings sites. In LGN, the measured RF distance was significantly
75 shorter for nearby cell pairs (4.8°±2.3°, median ± median absolute deviation; N=150 from 11
76 mice; **Fig. 2C**) than for distant cell pairs (14.0°±5.8°; N=4341 from 17 mice; p(U-test)<0.001;
77 **Fig. 2D**). In contrast, we found no statistically significant difference in OT (22.5°±15.8°, N=42
78 nearby pairs from 18 mice, **Fig. 2A**; 28.9°±12.3°, N=767 distant pairs from 33 mice, **Fig. 2B**;
79 p(U-test)=0.14). This indicates that neighboring RGC axons in the mouse OT do not
80 necessarily have adjacent RFs, violating the definition of retinotopy.

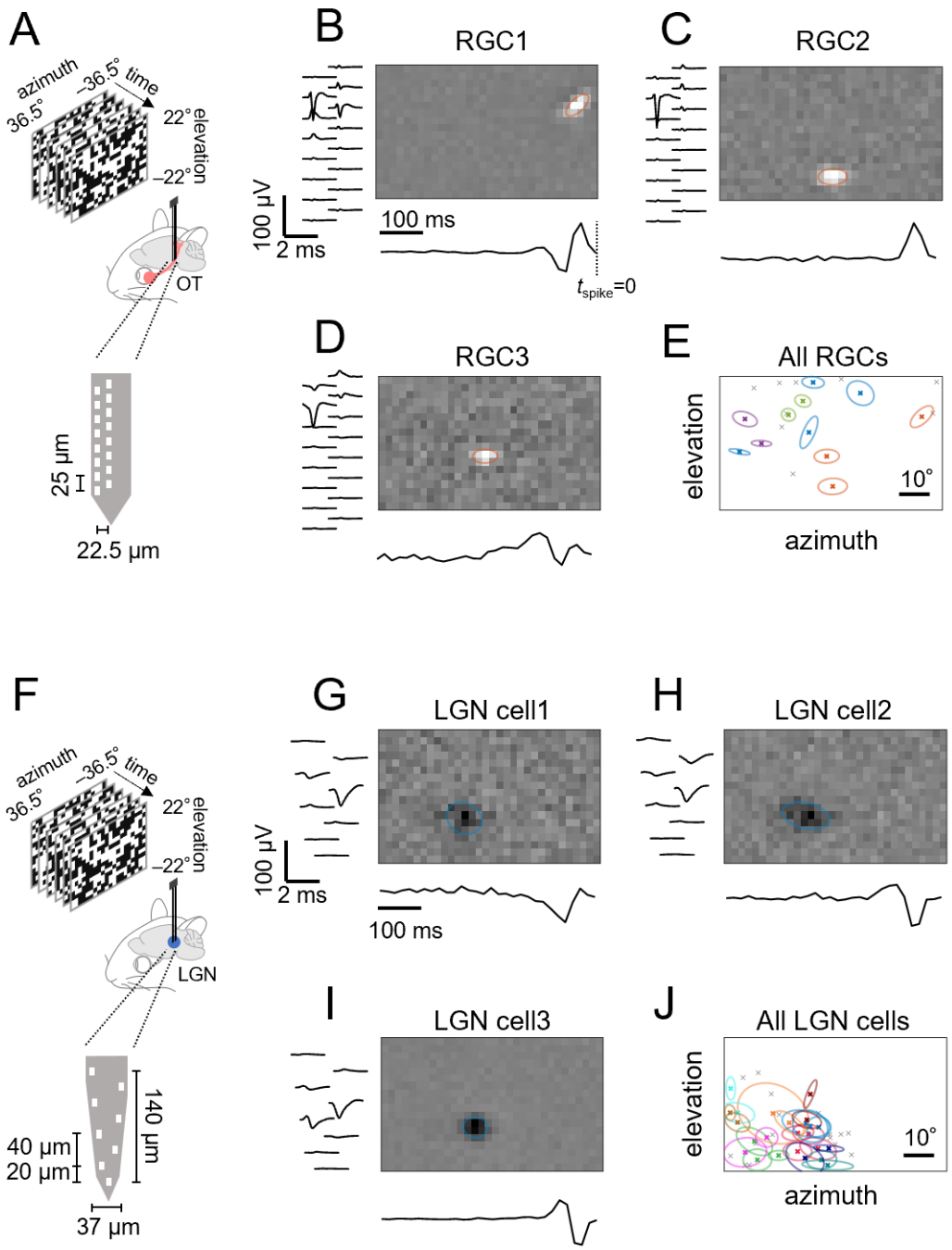

Figure 1: Receptive fields (RFs) of retinal ganglion cell (RGC) axons simultaneously recorded in the mouse optic tract (OT) are more widely spread across the visual field than those of lateral geniculate nucleus (LGN) cells. A: Schematic of OT recordings in awake head-fixed mice. B–D: Spatial RF (top) and temporal kernel (bottom) of three representative single-units that had the largest signals on the same recording site from a representative OT recording (left, average spike waveform in each recording site). Orange ellipses show a two-dimensional Gaussian envelope (at 1.5σ) fitted to the spatial RF profile of each unit. E: RF center locations of all simultaneously recorded single-units from the representative OT recording (crosses). Those with the largest signals on the same recording site are shown with the Gaussian envelopes of the same color. F–J: Corresponding data for a representative LGN recording (F, schematic; G–I, spatial RF, temporal kernel, and spike waveforms of three representative units that had the largest signals on the same recording site; J, RF center locations of all simultaneously recorded single-units).

To further support this claim, we took a modelling approach to estimate an expected RF distance for nearby cell pairs given retinotopy (see Methods for details), and compared it to the measured RF distance. For nearby LGN cell pairs, Monte Carlo simulations yielded an estimated RF distance between 4.2° and 4.9° (95% confidence interval; median, 4.6°; **Fig. 2C**), given the retinotopy gradient of 0.11°/μm (Piscopo et al., 2013) and a reliable single-unit recording range of 40 μm from an extracellular electrode (Anastassiou et al., 2015). This is consistent with the measured RF distance (median, 4.8°), validating our modelling approach. For nearby RGC axon pairs in the mouse OT (diameter, ~300 μm; visual field extending ~135° in both azimuth and elevation; Paxinos and Franklin, 2001), our model demonstrated that the median RF distance should range from 7.9° to 10.7° (95% confidence interval; median, 9.3°; **Fig. 2A**) if RGC axons were aligned retinotopically in the OT. This disagreed with the measured RF distance (median, 22.5°), hence rejecting the presence of retinotopy imposed as a key premise of the model.

To what extent does the mouse OT retain topographic organization? To address this question, we extended our model by introducing additive Gaussian noise to the RF location of the simulated RGC axons (see Methods for details), where σ=1 corresponds to the represented visual field (135°). We then used Kendall's τ as a measure of spatial monotonicity to quantify the degree of retinotopy, where τ=1 and 0 represent precise and no retinotopy, respectively. As expected, the retinotopy level τ decreased with increasing noise level σ, and the estimated RF distance of nearby RGC axons expanded (**Fig. 2E,F**). From the intersection between the measured and simulated RF distances, we then identified that the mouse OT had a moderate level of retinotopy (τ=0.45) with σ=0.15, corresponding to a deviation of RF location from a retinotopically ideal position by ~20°, or equivalently, a displacement of RGC axons by ~45 μm (**Fig. 2G,H**). This indicates that the mouse OT lacks local retinotopy, while maintaining topographic organization at a global level.

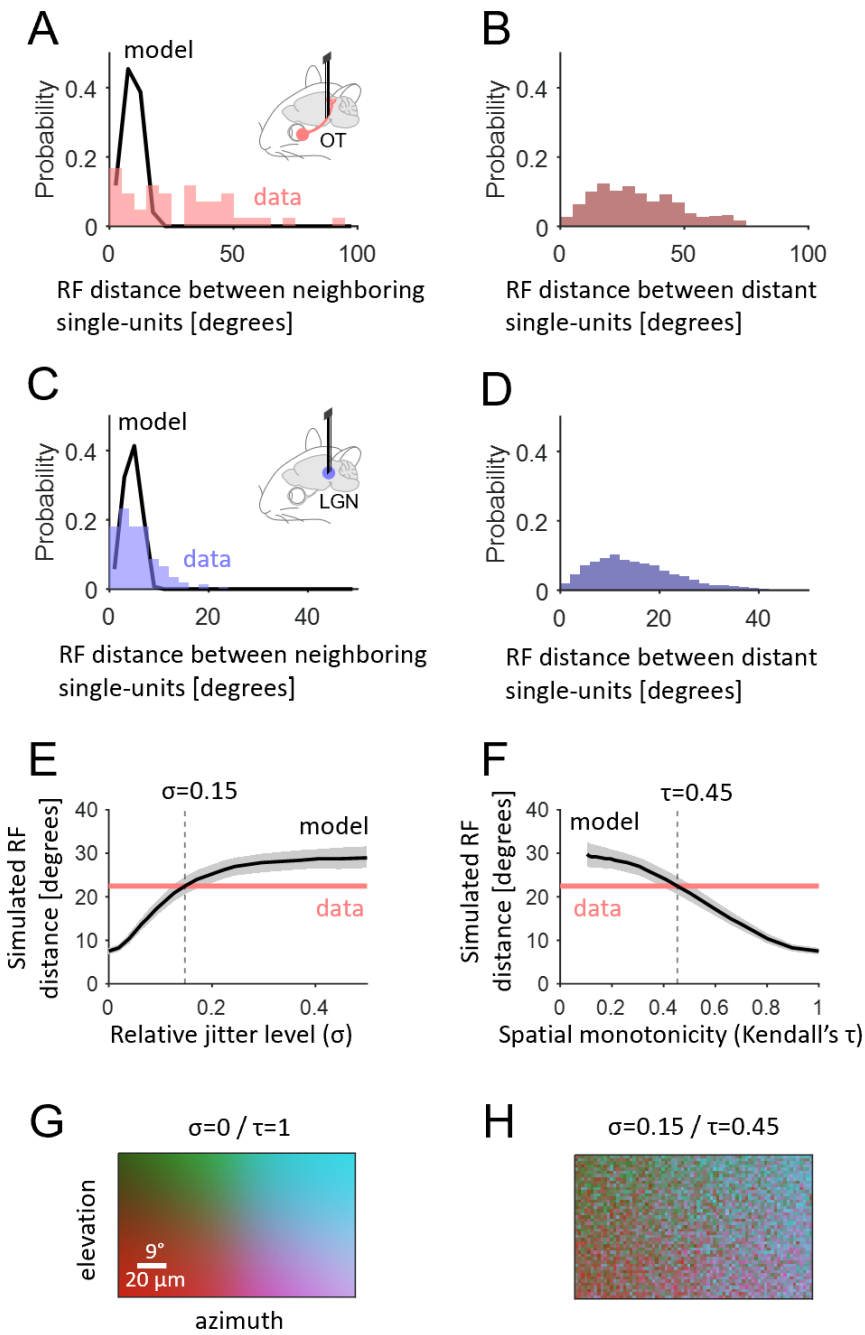

Figure 2: The mouse optic tract (OT) lacks local topographic organization, while maintaining global retinotopy. A,B: Probability distribution of the RF center distance between RGC axons in the mouse OT (histograms; A, N=42 neighboring pairs with the largest signals on the same recording site from 18 animals; B, N=767 distant pairs with the largest signals on different recording sites from 33 animals), and the expected distribution by Monte Carlo simulation (A, line). C,D: Corresponding data for LGN cells (C, N=150 neighboring pairs from 11 animals (histogram) and Monte Carlo simulation (line); D, N=4341 distant pairs from 17 animals). E,F: Simulated RF distance between nearby RGC axons at different retinotopy levels. Additive Gaussian noise (at different jitter levels, σ; E) was introduced to RF locations to achieve different spatial monotonicity levels (Kendall's τ) of their topographic organization (F): black line, median; gray shade, 25 and 75 percentile range; black dotted line, expected σ and τ values given the measured data (red). G,H: Simulated topographic map (color-coded) of the mouse OT with precise retinotopy (G), or at a moderate level of spatial monotonicity as identified from the experimental data (H).

Discussion

Here we provide in vivo electrophysiological evidence for the absence of local retinotopy in the mouse optic tract (OT). Both population-level analyses and data-driven models failed to identify a fine-scale topographic organization in the OT that would make neighboring retinal ganglion cell (RGC) axons encode adjacent locations in the visual field. In contrast, corresponding analyses on the dorsal lateral geniculate nucleus (LGN) supported the presence of retinotopy as expected from previous studies (Huberman et al., 2008; Seabrook et al., 2017), thereby serving as a control for our functional circuit characterization.

While the OT is largely intermingled to form a broad retinotopy, there is partial and graded segregation of RGC axons by the cell type and projection target (Erskine and Herrera, 2014; Robles et al., 2014). Our models did not incorporate this typology, and thus may underestimate the actual degree of retinotopy in OT. Another caveat of our results lies in our assumption that single-units with the largest signals on the same recording site should be adjacent to each other. Although this is generally expected, it may not always hold for OT recordings because RGC axons have internode lengths of ~140 μm (Butt et al., 1994). This means that nodes of Ranvier from neighboring axons can be offset by up to ~70 μm, potentially leading their signals to be maximally detected by different recording sites. Nevertheless, nearby units as defined here should still be in close proximity to a given recording site, and thus near each other if not the closest. This guarantees the validity and robustness of our data/model analyses.

Our finding that RGC axons in the mouse OT are only coarsely segregated implies a fundamental constraint of early visual pathway organization: i.e., pre-target axon sorting cannot maintain or recover precise spatial relationships over long distances (Plas et al., 2005). This is consistent with the known limits of axon guidance mechanisms, such as Eph/ephrin signaling and axon fasciculation, that establish broad topographic gradients but lack the resolution to ensure single-axon positional fidelity (McLaughlin and O'Leary, 2005; Cang and

Feldheim, 2013). Consequently, fine retinotopy must be re-established within each target via activity-dependent mechanisms—including spontaneous retinal waves and Hebbian learning—to impose local precision on coarse inputs (Debski and Cline, 2002; McLaughlin et al., 2003). This two-step architecture likely reflects an adaptive circuit organization principle: by relaxing long-range wiring constraints, the system reduces developmental cost while increasing robustness. Small positional deviations in the OT, for example, have minimal impact because final mappings are refined locally in individual targets. Moreover, each area remains free to optimize the retinotopic map for its own computational needs (Knapen, 2021), rather than relying on the geometric arrangement of incoming axons themselves. Testing these functional implications in the visual system—and examining if they extend across the central nervous system—will be an important next step in future studies.

Materials and Methods

No statistical method was used to predetermine the sample size. The significance level was 0.05 in all analyses unless otherwise noted. All experiments were performed under the license 233/2017-PR and 220/2024-PR from the Italian Ministry of Health, following protocols approved by the Institutional Animal Care and Use Committee at European Molecular Biology Laboratory. The data analyses were done in Python and Matlab.

Animals

Animals were housed on a 12h light-dark cycle, with ad libitum access to water and food. In total, 50 female wild-type mice (C57BL6/J; RRID:IMSR_JAX:000664), 4-19 weeks old (median, 9.2 weeks old) at the time of surgery, were used for in vivo electrophysiology (optic tract, 33 animals; lateral geniculate nucleus, 17 animals).

In vivo electrophysiology

In vivo electrophysiology was performed as described previously (Tripodi and Asari, 2025). Briefly, we first implanted a head-plate to animals for fixing their head during in vivo

186 electrophysiological recordings. Before the surgery, animals were injected with Carprofen (5
187 mg/kg) and then anaesthetized with isoflurane (4% for induction, 1% for maintenance in O_2).
188 During the surgery, the animals were placed in a stereotaxic frame (Stoelting 51625) with a
189 heating pad (Supertech Physiological) to keep their temperature stable at 37°C; and ointment
190 (VitA-Pos, Ursapharm) was applied on both eyes to prevent them from drying. A portion of the
191 scalp was removed to expose the skull, and the periosteum was scraped away with a round
192 scalpel to increase adherence of the dental cement. A titanium head-plate with a hole
193 (diameter, 8mm) was then cemented on the skull with a mixture of cyanoacrylate (Loctite 401,
194 Henkel) and dental cement (Paladur, Kulzer). The skull surface was then glazed with a thick
195 layer of cyanoacrylate to support the skull with mechanical, atmospheric and biological
196 protection, while still allowing for visual identification of reference points (bregma and lambda).
197 After the surgery, the animals were placed on a heating pad for recovery, and then housed in
198 individual cages. During the following seven days, the mice were administered with analgesia
199 (Carprofen; 50 mg/mL) diluted in drinking water.

200 After recovery from the surgery, the animals were habituated to head fixation on the
201 experimental apparatus for one week (twice a day for up to two hours). On the day of the
202 recording, we first placed the subject animal in the recording set up with its head fixed, and
203 determined the electrode penetration path to the target area (optic tract, [-1.34, +1.87, +4.74],
204 [-1.70, +1.87, +4.74], or [-1.82, +2.35, +4.07] in [anterior-posterior (AP), medial-lateral (ML),
205 dorsal-ventral (DV)] coordinates; LGN, [-2.3, +2.3, +2.8]) using the robotic stereotaxic system
206 (StereoDrive, NeuroStar). The animal was then briefly anesthetized with isoflurane for about
207 5 minutes, and a hole was drilled around the electrode entry point on the skull. After the
208 removal of the anesthesia, an acute silicone probe (P2, Cambridge Neurotech, **Fig. 1A**; or
209 Buzsaki32L, Neuronexus, **Fig. 1F**) coated with a fluorescent dye (DiI stain, Invitrogen, D282)
210 was lowered at 5 μm/s using the robotic arm until visual responses were found in the target
211 area. A battery of visual stimuli (see below for details) were then presented for recordings.

212 After the recording session, the electrode position was verified histologically. After
213 retracting the silicon probe, the mice were anesthetized (2.5% Avertin, 16 μL/g, intraperitoneal
214 injection) and perfused with paraformaldehyde (PFA; 4% in phosphate buffer solution),
215 followed by brain tissue harvest and overnight post-fixation in 4% PFA at 4°C. Coronal
216 sections of the brain tissue (thickness, 100-150 μm) were then examined under a fluorescence
217 microscope (Leica, LMD7000 with N2.1 filter cube) to visualize the trace left by the DiI stain
218 on the probe.

219 Visual stimulation

220 Visual stimuli were presented as described before (Boissonnet et al., 2023). Briefly, visual
221 stimuli were projected to a spherical screen (radius, 20 cm) placed ~20 cm from the animal's
222 left eye, covering about a quarter of its visual field (±36.5° and ±22° in azimuth and elevation,
223 respectively). A gamma-corrected digital light processing device (Texas Instruments,
224 DLPDLCR3010EVM-LC) was used as a light source, where the green and the red light-
225 emitting diodes (LEDs) were replaced with ultraviolet (UV; 365nm, LZ1-00UV00, LED Engine)
226 and infrared (IR; 950nm, SFH 4725S, Osram) LEDs, respectively. The UV and remaining blue
227 channels were used for visual stimulation (frame rate, 60 Hz; maximum intensity, 31 mW/m^2),
228 while the IR signals were recorded with a photodiode (PDA100A2, Thorlabs) for data
229 synchronization. For receptive field (RF) mapping, a black-and-white binary noise stimulus
230 was presented for 15 minutes, consisting of a 32-by-18 pixels checkerboard patterns, where
231 each pixel randomly and independently flickered at 60 Hz while keeping the overall luminance
232 of each frame constant at the mean intensity.

233 Data analysis

234 We adapted previously established methods of spiking sorting and data analysis (Boissonnet
235 et al., 2023; Tripodi and Asari, 2025). In brief, we used Kilosort 2.0 to sort spikes with a set of
236 default parameters, except for the spike detection threshold to be 6 during optimization.
237 Single-units were then identified by clustering in principal component space using Phy for

visualization and manual data curation. Only those units that maintained the average spike waveforms and autocorrelograms with a minimal refractory period of 1 ms were kept for subsequent analyses.

For the visual RF analysis, we employed stimulus ensemble statistical techniques (reverse correlation methods; 500 ms window; Δt = 1/60 s bin size). Specifically, we first obtained the linear spatiotemporal RF of each recorded cell by calculating a spike-triggered average (STA) of the "checkerboard" stimuli with ±1 being "white" and "black" for each pixel, respectively. As a quality measure, *p*-value was computed for each voxel against a null hypothesis that the STA follows a normal distribution $N(0, 1/C)$, where C is the total number of spikes. For those with $p < 10^{-5}$ at any voxel, we ran a singular value composition to obtain temporal and spatial filters, respectively, assuming the separability of RGC/LGN spatiotemporal RFs. We then fitted a two-dimensional Gaussian envelope to those spatial filters with a single, distinct and localized feature; and considered the center of the Gaussian as the RF center location (**Fig. 1**).

To a first approximation, at short distances, the amplitude of extracellular signals is inversely proportional to the distance between the cell and the probe (Anastassiou et al., 2015). We thus considered that the recorded units were physically located nearby if they both had the largest spike waveforms on the same recording site on the probe, whereas distant if they had the largest spike waveforms on different recording sites. Using these criteria, we identified pairs of nearby and distant single-units that were recorded simultaneously (optic tract, 42 and 767 pairs in total, respectively; LGN, 150 and 4341 pairs in total, respectively), and compared the distance between their RF center locations at the population level using Mann-Whitney U-test (**Fig. 2**).

Model analysis

We used Monte Carlo methods to obtain an expected RF distance distribution of nearby cell pairs, given a retinotopy gradient *g*. In particular, we first randomly sampled two points in a

sphere, where the radius *r* represents the maximum distance from an extracellular electrode for reliable single-unit recording. If the distance between the two points, *D*, was larger than an exclusion threshold *d* due to a physical mass of neurons, we then estimated the RF distance between two neurons located at those two sampled points as $D \times g$. We repeated the procedure $1000n$ times to compute the probability distribution function of the estimated RF distance, as well as a 95% confidence interval of the median value (of sample size *n*). For the mouse OT (*n* = 42; **Fig. 2A**), we used *r* = 20 μm for recording range, *d* = 2 μm for RGC axon diameter, and *g* = (represented visual field) / (optic tract diameter) = 135° / 300 μm (Paxinos and Franklin, 2001). For the mouse LGN (*n* = 150; **Fig. 2C**), we used *r* = 40 μm for recording range, *d* = 10 μm for cell body size, and *g* = 0.11°/μm (Piscopo et al., 2013).

To run simulations at different retinotopy levels for the mouse OT (**Fig. 2E-H**), we added noise to the simulated RF locations, drawn from a Gaussian distribution $N(0, \sigma^2)$ where σ=1 corresponds to the full range of the represented visual field (135°), or equivalently, the full width of the mouse OT (300 μm; Paxinos and Franklin, 2001). Simulations were done with σ=[0, 0.5] in steps of 0.05, as described above except that we randomly sampled two points within the distance *d* from a randomly chosen probe position within the visual stimulation area (73° and 44° in azimuth and elevation, respectively), and eliminated a trial if any cell on those two sampled points had its RF outside the visual stimulation area due to the added jitter. With increasing jitter, the simulated RF distance increased and the topographic map exhibited greater disorganization. To quantify the level of retinotopy, we used Kendall's τ as a measure of spatial monotonicity, where τ=0 indicates a random mapping with no retinotopy; and τ=1 represents a perfect retinotopy. The intersection between the measured and the simulated RF distances was then used to estimate the level of retinotopic organization in the mouse OT.

References

Anastassiou, C.A., Perin, R., Buzsáki, G., Markram, H., Koch, C. (2015). Cell type- and activity-dependent extracellular correlates of intracellular spiking. J Neurophysiol, 114(1), 608 – 623.

291 Boissonnet, T., Tripodi, M., Asari, H. (2023). Awake responses suggest inefficient dense
292 coding in the mouse retina. Elife. 12, e78005.

293 Bunt, S.M., Horder, T.J. (1983) Evidence for an orderly arrangement of optic axons within
294 the optic nerves of the major nonmammalian vertebrate classes. J Comp Neurol. 213(1),
295 94–114.

296 Butt, A.M., Colquhoun, K., Tutton, M., Berry, M. (1994). Three-dimensional morphology of
297 astrocytes and oligodendrocytes in the intact mouse optic nerve. J Neurocytol. 23(8), 469–
298 485.

299 Cang, J., Feldheim, D.A. (2013) Developmental mechanisms of topographic map
300 formation and alignment. Annu Rev Neurosci. 36, 51–77.

301 Cang, J., Savier, E., Barchini, J., Liu, X. (2018) Visual Function, Organization, and
302 Development of the Mouse Superior Colliculus. Annu Rev Vis Sci. 4, 239–262.

303 Colello, S. J., Guillery,R. W. (1998) The changing pattern of fibre bundles that pass through
304 the optic chiasm of mice. Eur. J. Neurosci. 10, 3653–3663.

305 Debski, E.A., Cline, H.T. (2002) Activity-dependent mapping in the retinotectal projection.
306 Curr Opin Neurobiol. 12(1), 93–99.

307 Erskine, L., Herrera, E. (2014) Connecting the retina to the brain. ASN Neuro. 6(6),
308 1759091414562107.

309 Horton, J.C., Greenwood, M.M., Hubel, D.H. (1979) Non-retinotopic arrangement of fibres
310 in cat optic nerve. Nature. 282(5740), 720–722.

311 Huberman, A.D., Feller, M.B., Chapman, B. (2008) Mechanisms underlying development
312 of visual maps and receptive fields. Annu Rev Neurosci. 31, 479–509.

313 Imai, T., Yamazaki, T., Kobayakawa, R., Kobayakawa, K., Abe, T., Suzuki, M., Sakano, H.
314 (2009) Pre-target axon sorting establishes the neural map topography. Science. 325(5940),
315 585–590.

316 Jeffery, G. (2001). Architecture of the optic chiasm and the mechanisms that sculpt its
317 development. Physiol Rev. 81(4), 1393–1414.

318 Knapen, T. (2021) Topographic connectivity reveals task-dependent retinotopic
319 processing throughout the human brain. Proc Natl Acad Sci U S A. 118(2), e2017032118.

320 Marcus, R.C., Mason, C.A. (1995) The first retinal axon growth in the mouse optic chiasm:
321 axon patterning and the cellular environment. J Neurosci. 15(10), 6389–6402.

322 Martersteck, E.M., Hirokawa, K.E., Evarts, M., Bernard, A., Duan, X., Li, Y., Ng, L., Oh,
323 S.W., Ouellette, B., Royall, J.J., Stoecklin, M., Wang, Q., Zeng, H., Sanes, J.R., Harris,
324 J.A. (2017) Diverse Central Projection Patterns of Retinal Ganglion Cells. Cell Rep. 18(8),
325 2058–2072.

326 McLaughlin, T., Torborg, C.L., Feller, M.B., O'Leary, D.D.M. (2003) Retinotopic map
327 refinement requires spontaneous retinal waves during a brief critical period of development.
328 Neuron. 40(6), 1147–1160.

329 McLaughlin, T., O'Leary, D.D.M. (2005) Molecular gradients and development of
330 retinotopic maps. Annu Rev Neurosci. 28, 327–355.

331 Molotkov, D., Ferrarese, L., Boissonnet, T., Asari, H. (2023). Topographic axonal
332 projection at single-cell precision supports local retinotopy in the mouse superior colliculus.
333 Nat Commun. 14(1), 7418.

334 Morin, L.P., Studholme, K.M. (2014). Retinofugal projections in the mouse. J. Comp.
335 Neurol. 522(16), 3733–3753.

336 Paxinos, G. and Franklin, K.B.J. (2001) The Mouse Brain in Stereotaxic Coordinates. 2nd
337 Ed., Academic Press, San Diego.

338 Piscopo, D.M., El-Danaf, R.N., Huberman, A.D., Niell, C.M. (2013). Diverse visual features
339 encoded in mouse lateral geniculate nucleus. J Neurosci. 33(11), 4642–4656.

340 Plas, D.T., Lopez, J.E., Crair, M.C. (2005). Pretarget sorting of retinocollicular axons in the
341 mouse. J Comp Neurol. 491(4), 305–319.

342 Reese, B.E. (2011) Development of the retina and optic pathway. Vision Res. 51(7), 613–
343 632.

344 Robles, E., Laurell, E., Baier, H. (2014). The retinal projectome reveals brain-area-specific
345 visual representations generated by ganglion cell diversity. Curr Biol. 24(18), 2085–2096.

346 Seabrook, T.A., Burbridge, T.J., Crair, M.C., Huberman, A.D. (2017). Architecture,
347 Function, and Assembly of the Mouse Visual System. Annu Rev Neurosci. 40, 499–538.

348 Sitko, A.A., Kuwajima, T., Mason, C.A. (2018) Eye-specific segregation and differential
349 fasciculation of developing retinal ganglion cell axons in the mouse visual pathway. J
350 Comp Neurol. 526(7), 1077–1096.

351 Tripodi, M., Asari, H. (2025). The central histaminergic system slows visual processing in
352 the retina and lateral geniculate nucleus of awake mice. PLoS Biol. 23(11), e3003406.

Zhou, J., Wen, Y., She, L., Sui, Y.-N., Liu, L., Richards, L.J., Poo, M.-M. (2013). Axon position within the corpus callosum determines contralateral cortical projection. Proc Natl Acad Sci U S A. 110(29), E2714 – E2723.